Improvement of Hydrogen Storage by Adsorption Using 2-D Modeling of Heat Effects

A. Delahaye, A. Aoufi, and A. Gicquel
Laboratoire d'Ingénierie des Matériaux et Hautes Pressions, CNRS UPR 1311 - Université Paris 13, 93430 Villetaneuse, France

I. Pentchev
Dépt. de Génie Chimique–UCTM, 8, 1756 Sofia, Bulgaria

The use of hydrogen storage based on an adsorption process for cars operating on a fuel cell will be seriously considered when the amount of stored gas is high enough, the tank safe and economically viable, and the filling process fast enough. To maximize the storage capacity for rapid filling, it is necessary to minimize heating of the adsorbent bed and to imagine means to extract energy toward the outside. Numerical simulation of such a hydrogen storage tank, based on a 2-D model where mass and thermal energy balances are coupled, is presented. Results from simulations agreed well with experiments, when various modified parameters were calculated. Solutions for improving adsorbent beds for hydrogen storage tanks are then proposed.

Introduction

Environmental problems linked to the emission of greenhouse-effect gases and to the depletion of fossil-fuel reserves has led the car industry to search for new means for powering and operating automobiles as well as public-transportation vehicles. During the coming century, gasoline should be replaced by a cleaner, renewable motor-fuel such as hydrogen while fuel cells should take the place of the internal combustion engine (Nicoletti, 1995; Das, 1996). However, it is necessary to review our current knowledge, in particular of hydrogen storage tanks, which must be safe, compact, and economically viable (Berry and Aceves, 1998; Noh et al., 1987; Hynek et al., 1997). Hydrogen storage by cryogenic liquefaction and by compression at very high pressure (70 MPa) is not yet considered viable due to safety problems or to high cost, and hydrogen storage by metal hydride is hampered by its weight and limited number of cycles.

Adsorption storage over much lower pressure (15 MPa) and at room temperature offers the advantage of considerably reduced risks linked to the use of very high pressure and of reduced costs due to cooling down. In order to make this storage method viable, the adsorption capacity of the absorbent must be such as to allow storage, in a tank, of a sufficient amount of hydrogen for a car traveling over 500 km. According to the American Department of Energy standard (DOE), the tank must be able to store 63 kg/m^3 of hydrogen and to respect a mass standard of 6.5%, which corresponds to the ratio of the stored hydrogen mass to the total mass of the system (Dresselhaus et al., 1999). Moreover, the viability of this storage method requires very short filling times, typically of less than 5 min. Due to the exothermicity of the adsorption and compression processes, these low filling times cause an increase in the absorbent-bed temperature, which in turn limits the tank-gas density to a level lower than that which would be expected in the absence of adsorbent-bed heating.

The objective of the present work is to develop tools able to predict the thermal effects that occur in a hydrogen storage tank using an adsorption process and to propose solutions for reducing these effects. The thermal effects of adsorption have already been studied for pressure swing adsorption for gas-mixture separation using the Equilibrium

Correspondence concerning this article should be addressed to A. Delahaye.

Theory (Farooq and Ruthven, 1990), the linear driving force approximation (Chihara and Suzuki, 1983; Farooq et al., 1988; Kikinides and Yang, 1993) and taking into account intraparticle mass transfer (Zhong et al., 1992). The main difference between the PSA and gas storage processes is the higher pressure for the storage process and the existence of only one component. A 2-D model was developed in the past to calculate the thermal effects caused by methane storage (Barbosa, 1995; Barbosa et al., 1997), and work has recently been carried out in our laboratory (Lamari et al., 2000; Lamari, 2000) concerning hydrogen storage. This work enabled us to simulate thermal effects on the axis of the tank during the filling stage through the development of a 1-D model based on a PSA process in a long cylindrical tube (Farooq et al., 1988; Kikinides and Yang, 1993). The influence of various parameters, such as filling time and pressure, on the variations in the maximum temperature has been analyzed. However, this simulation obviously could not reproduce radial temperature distribution, and therefore was not appropriate for finding solutions for reducing the maximal temperature reached.

In order to have access to radial temperature distribution, a two-dimensional (2-D) model has recently been developed. We present here the model that describes mass and thermal transport phenomena arising in a cylindrical reactor, contains an adsorbent bed, and that undergoes hydrogen filling at room temperature, at various pressures. Numerical simulation, based on this 2-D model, provides radial and axial temperature profiles and allows us to test various parameters with the objective of finding those that determine the steepness of the gradients, in particular on the radius.

Experimental Setup

The experimental setup presented in Figure 1 is composed of four parts: the storage tank, the charge circuit, the discharge circuit, and the data-acquisition system.

The storage tank is a cylindrical stainless-steel column, with internal and external diameters of 96 mm and 125 mm, respectively, and an internal length of 255 mm. It is equipped with five thermocouples placed at various locations in order to measure axial and radial temperature fields. The base of the column is also equipped with a pressure transducer, capable of measuring pressures up to 25 MPa with an accuracy of $5 \cdot 10^{-3}$ MPa. At the top of the column, the entry is sealed with an insulating tap. The tank is filled with an adsorbent in the form of small grains having an average diameter of 2 mm. The nature of the adsorbent can be changed. For validation of the model, incinerated activated coconut coal produced by Professor R. Chahine's group ("Institut de Recherche sur l'Hydrogène," Quebec) was used.

The filling circuit is composed of an 8.8 m^3 hydrogen bottle (at 20 MPa; purity: 99.99%), equipped with a pressure regulator, linked through a pipe to the tank. The hydrogen flow rate entering the tank is measured using a volumetric flow meter. Downstream from the flowmeter, a throttle valve is used to control the hydrogen flow with an accuracy of $\pm 0.3\%$. Finally, a pneumatic control valve is used to regulate the introduction of gas into the tank.

In order to pump out the entire device, a primary pump is linked to a discharge circuit through a manual valve. The data-acquisition system includes a Keithley 2000 linked to the thermocouples and to the flowmeters. The temperature and flow-rate values can thus be read directly on a personal computer. The pressure transducer is directly connected to the computer.

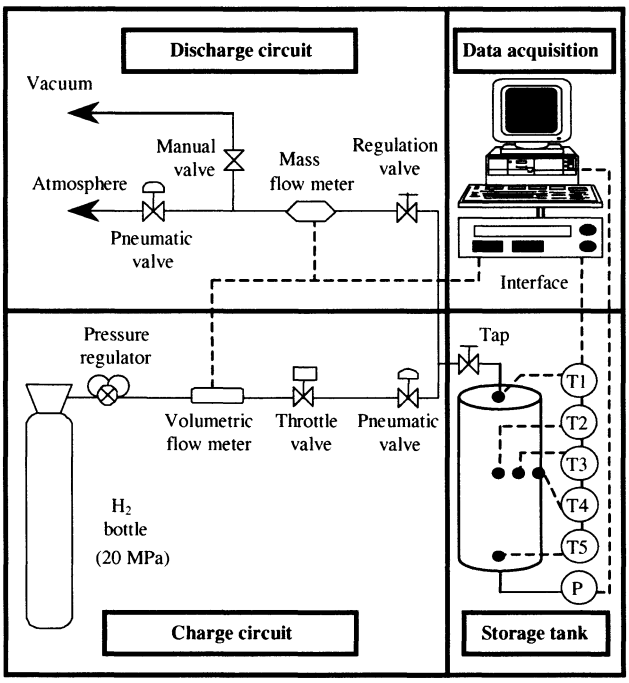

Figure 1. Experimental setup for storage.

Operating Principle

Before all filling operations, the flow-rate control must be adjusted. First, the filling pressure is set at a given value using the pressure regulator, and the pipe is then opened onto the outside using two pneumatic valves. The throttle valve is then activated in order to obtain the desired flow rate. Once this has been set up, the pneumatic valves are closed. This stage is crucial because the flow rate will determine the filling time. The residual gas present between the insulating tap of the tank and the two valves is then pumped out by the primary pump. Once the exhaust-pipe control valve is closed, the insulating tap is opened.

In the filling stage, the pneumatic command valve of the filling pipe is activated. Hydrogen then enters the tank at the previously determined flow rate. Temperature variations at various locations in the tank, as well as pressure, can be measured using the acquisition system.

Figure 2 shows the temperature variations at various locations during the filling operation performed at 15 MPa in 300 s. As shown in Figure 1, thermocouple T1 is located at the entrance of the column, while thermocouples T2, T3, and T4 are located halfway down the column. T2 is located in the center of the column, T3 is halfway along the radius, and T4 is at the column wall. Finally, thermocouple T5 is located at the end of the column.

Filling the tank is shown to increase the temperature significantly, by 60 K at the hottest location, that is, on the axis, at midheight. The vertical dotted line represents the final fill-

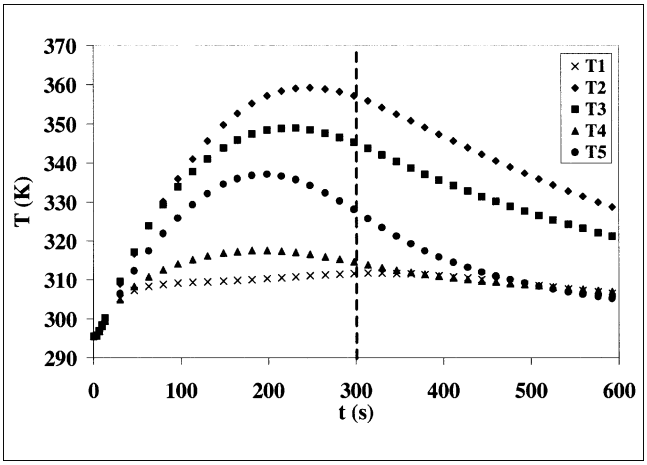

Figure 2. Temperature history at various positions in the column, at a charge pressure of 15 MPa and a charge time of 300 s.

ing time, that is, the time at which the flow rate reaches zero. The temperature distributions go over maximum even before the end of the filling. This behavior is attributed to the fact that the flow rate strongly decreases at the end of the filling stage and the pressure in the tank then increases less rapidly. At a certain threshold, exothermic adsorption and compression phenomena, which are highly correlated to pressure, are not able to compensate for heat transfer toward the walls. As a result, there is a time shift between the maximum temperature reached by the adsorbent bed and the end of the filling stage. However, although the temperature decreases slightly, it remains somewhat high, leading to a limitation in the amount of hydrogen that can be stored. The hydrogen density inside the tank is about 10% less than what would be expected in the absence of heating.

Description of the Mathematical Model

The two-dimensional pseudohomogeneous mathematical model of an activated carbon fixed bed filled by hydrogen is based on mass and heat balances in an elementary volume, using a cylindrical coordinate system because of the cylindrical shape of the vessel. The mass balance is based on the Equilibrium Theory of adsorption (Knaebel and Hill, 1983, 1985; Ruthven et al., 1994). After some simplification, we obtain the following set of equations

$$\begin{cases} \dfrac{\partial}{\partial z}\left(D_{\mathrm{ax}}\dfrac{\partial \rho}{\partial z}-\rho\dfrac{u}{\epsilon}\right)+\dfrac{D_r}{r}\dfrac{\partial}{\partial r}\left(r\dfrac{\partial \rho}{\partial r}\right)=\dfrac{\partial \rho}{\partial t}+\dfrac{1-\epsilon}{\epsilon}\rho_s M_{\mathrm{H}_2}\dfrac{\partial q^*}{\partial t} & (1) \\ \dfrac{\partial}{\partial z}\left(\dfrac{\lambda_{\mathrm{ax}}}{\epsilon}\dfrac{\partial T}{\partial z}-\rho\dfrac{u}{\epsilon}C_pT\right)+\dfrac{\lambda_r}{\epsilon r}\dfrac{\partial}{\partial r}\left(r\dfrac{\partial T}{\partial r}\right)= & \\ \qquad \dfrac{\partial}{\partial t}\left(\rho C_pT+\dfrac{1-\epsilon}{\epsilon}\rho_s C_{ps}T-\rho\dfrac{RT}{M}\right)-\dfrac{1-\epsilon}{\epsilon}\rho_s\Delta H\dfrac{\partial q^*}{\partial t}. & (2) \end{cases}$$

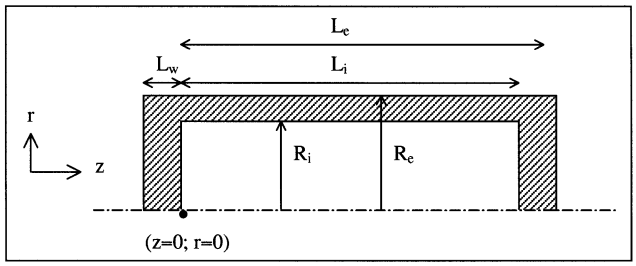

Figure 3. Section view of the tank.

According to the Equilibrium Theory of Adsorption, q^* is the quantity of adsorbed gas in equilibrium with the gas phase. It has been proven that when the kinetics are fast, the Equilibrium Theory gives satisfactory results (Zhong et al., 1992; Ruthven et al., 1994). In this case, the porosity used is higher than external porosity in order to take a part of the pores into account (Ruthven et al., 1994).

The initial conditions are based on the assumption that, at the beginning of the filling, the vessel does not contain any hydrogen and its temperature is equal to room temperature

$$t=0 \qquad \rho(z,r,0)=\rho_0; \qquad T(z,r,0)=T_{\mathrm{a}};$$
$$q^*(z,r,0)=q^*(P_0,T_a) \quad (3)$$

The following spatial notations for describing the boundary conditions are illustrated in the section view of the tank in Figure 3

$R_i < r < R_e$ and $-L_w < z < L_e$: cylindrical wall.

$-L_w < z < 0$ and $0 < r < R_e$: entrance cover.

$L_i < z < L_e$ and $0 < r < R_e$: end cover.

Remark. The term "walls" refers to these three zones.

The boundary conditions on the z-axis of the vessel assure the absence of mass and heat flow

$$r=0 \qquad \text{for} \qquad 0<z<L_i$$
$$\frac{\partial \rho}{\partial r}(z,0,t)=0 \quad (4)$$
$$\frac{\partial T}{\partial r}(z,0,t)=0. \quad (5)$$

The boundary conditions for the mass balance at the inner boundary of the tank are the following

$$r = R_i \qquad \text{for} \qquad 0 < z < L_i \text{ (inner cylindrical wall)}$$

$$\frac{\partial \rho}{\partial r}(z,R_i,t) = 0, \tag{6}$$

$z = 0$ for $0 < r < R_i$ (inner entrance cover: boundary conditions for the mass balance according to Dankwerts)

$$u(0,r,t)\,\rho(0,r,t) - \epsilon D_{\text{ax}} \frac{\partial \rho}{\partial z}(0,r,t) = u(0,r,t)\,\rho_T \tag{7}$$

$$z = L_i \qquad \text{for} \qquad 0 < r < R_i \text{ (inner end cover)}$$

$$\frac{\partial \rho}{\partial z}(L_i,r,t) = 0. \tag{8}$$

Heat transfer across the vessel walls can be expressed in two ways. The first, called "boundary conditions with an independent energy balance for the walls," considers various heat balances for the cylindrical wall and the covers. In this case, the heat balance can be written as follows

$$\rho_w C_{pw} \frac{\partial T_w}{\partial t} = \lambda_w \left[\frac{1}{r} \frac{\partial}{\partial r} \left(r \frac{\partial T_w}{\partial r} \right) + \frac{\partial^2 T_w}{\partial z^2} \right]. \tag{9}$$

At the inner boundary of the cylindrical wall, the boundary conditions for the heat balance are the following

$$r = R_i \qquad \text{for} \qquad 0 < z < L_i$$

$$-\lambda_r \frac{\partial T}{\partial r}(z,R_i,t) = -\lambda_w \frac{\partial T_w}{\partial r}(z,R_i,t) \tag{10}$$

$$T(z,R_i,t) = T_w(z,R_i,t). \tag{11}$$

At the external boundary of the cylindrical wall, the boundary conditions for the heat balance are

$$r = Re \qquad \text{for} \qquad -L_w < z < L_e$$

$$-\lambda_w \frac{\partial T_w}{\partial r}(z,R_e,t) = h\left[T_w(z,R_e,t) - T_a\right]. \tag{12}$$

At the inner boundary of the entrance cover, the boundary conditions for the heat balance according to Danckwerts are

$$z = 0 \qquad \text{for} \qquad 0 < r < R_i$$

$$u(0,r,t)\,\rho(0,r,t)C_p T(0,r,t) - \lambda_{\text{ax}} \frac{\partial T}{\partial z}(0,r,t) =$$

$$u(0,r,t)\,\rho_T C_p T_a - \lambda_w \frac{\partial T_w}{\partial z}(0,r,t) \tag{13}$$

$$T(0,r,t) = T_w(0,r,t). \tag{14}$$

At the external boundary of the entrance cover, the boundary conditions for the heat balance are

$$z = -L_w \qquad \text{for} \qquad 0 < r < R_e$$

$$\lambda_w \frac{\partial T_w}{\partial z}(-L_w,r,t) = h\left[T_w(-L_w,r,t) - T_a\right]. \tag{15}$$

At the inner boundary of the end cover, the boundary conditions for the heat balance are

$$z = L_i \qquad \text{for} \qquad 0 < r < R_i$$

$$-\lambda_{\text{ax}} \frac{\partial T}{\partial z}(L_i,r,t) = -\lambda_w \frac{\partial T_w}{\partial z}(L_i,r,t) \tag{16}$$

$$T(Li,r,t) = T_w(Li,r,t). \tag{17}$$

At the external boundary of the end cover, the boundary conditions for the heat balance are

$$z = L_e \qquad \text{for} \qquad 0 < r < R_e$$

$$-\lambda_w \frac{\partial T_w}{\partial z}(L_e,r,t) = h\left[T_w(L_e,r,t) - T_a\right]. \tag{18}$$

For the two covers, the boundary conditions on the z-axis assure the absence of heat flow:

$$r = 0 \qquad \text{for} \qquad -L_w < z < 0 \qquad \text{and for} \qquad L_i < z < L_e$$

$$\frac{\partial T_w}{\partial r}(z,0,t) = 0. \tag{19}$$

Thus, the equations for mass and heat balances in the bed and for the heat balances in the cylindrical wall and in the two covers are simultaneously resolved. Axial and radial profiles are illustrated in Figures 4 and 5, respectively.

The second way to express heat flow across the cylindrical wall and the covers, called "integrated boundary conditions," requires that the heat balance (Eq. 9) for the cylindrical wall and the covers in the boundary conditions of the bed at the inner side of the tank be included, assuming a uniform temperature throughout the thickness of the walls (Zoghlami-Mosrati, 1999). The number of equations can thus be reduced, as well as the size of the grid built for the numerical simulation. The heat balance is integrated for the cylindrical wall between R_i and R_e, for the entrance cover between $-L_w$ and 0, and for the end cover between L_i and L_e: after integration for the cylindrical wall

$$\text{for} \qquad -L_w < z < L_e$$

$$R_e \lambda_w \frac{\partial T_w}{\partial r}(z,R_e,t) - R_i \lambda_w \frac{\partial T_w}{\partial r}(z,R_i,t) + \lambda_w \int_{R_i}^{R_e} \frac{\partial^2 T_w}{\partial z^2} r\,dr$$

$$= \rho_w C_{pw} \frac{\partial \int_{R_i}^{R_e} T_w r\,dr}{\partial t} \tag{20}$$

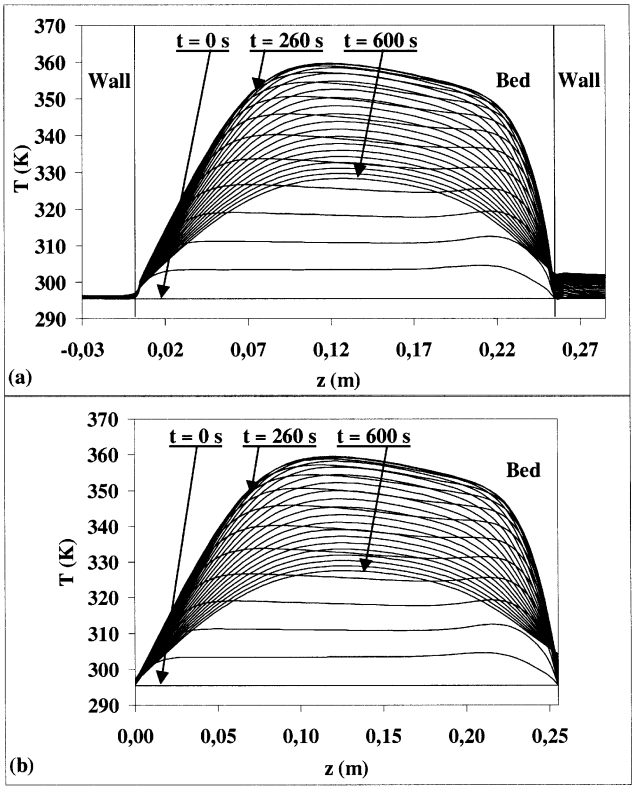

Figure 4. Axial profiles over 600 s, at a charge pressure of 15 MPa and a charge time of 300 s: (a) independent energy balance for the wall; (b) integrated boundary conditions.

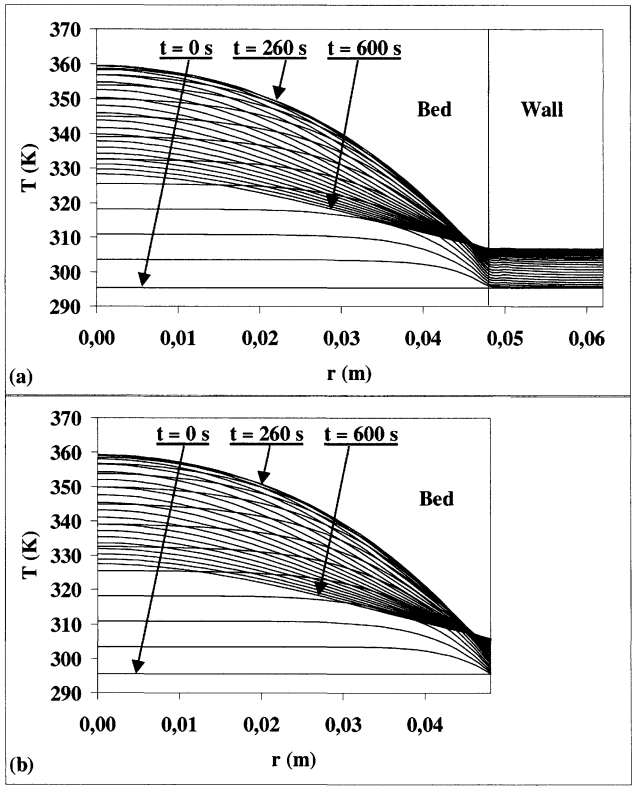

Figure 5. Radial profiles over 600 s, at a charge pressure of 15 MPa and a charge time of 300 s: (a) independent energy balance for the wall; (b) integrated boundary conditions.

after integration for the entrance cover

$$\text{for} \qquad 0 < r < R_e$$

$$\lambda_w \frac{\partial T_w}{\partial z}(0,r,t) - \lambda_w \frac{\partial T_w}{\partial r}(-L_w,r,t) + \lambda_w \int_{-L_w}^{0} \frac{1}{r}\frac{\partial}{\partial r}\left(r\frac{\partial T_w}{\partial r}\right) dz = \rho_w C_{pw} \frac{\partial \int_{-L_w}^{0} T_w \, dz}{\partial t} \quad (21)$$

after integration for the end cover

$$\text{for} \qquad 0 < r < R_e$$

$$\lambda_w \frac{\partial T_w}{\partial z}(L_e,r,t) - \lambda_w \frac{\partial T_w}{\partial r}(L_i,r,t) + \lambda_w \int_{L_i}^{L_e} \frac{1}{r}\frac{\partial}{\partial r}\left(r\frac{\partial T_w}{\partial r}\right) dz = \rho_w C_{pw} \frac{\partial \int_{L_i}^{L_e} T_w \, dz}{\partial t}. \quad (22)$$

We use the following assumption for T_w

$R_i < r < R_e$ and $-L_w < z < L_e$: for the cylindrical wall

$$T_w(z,R_i,t) = T_w(z,r,t) = T_w(z,R_e t) \quad (23)$$

$-L_w < z < 0$ and $0 < r < R_e$: for the entrance cover

$$T_w(-L_w,r,t) = T_w(z,r,t) = T_w(0,r,t) \quad (24)$$

$L_i < z < L_e$ and $0 < r < R_e$: for the end cover

$$T_w(L_i,r,t) = T_w(z,r,t) = T_w(L_e,r,t). \quad (25)$$

Equations 10, 11, and 12 for the cylindrical wall, Eqs. 13, 14, and 15 for the entrance cover, and Eqs. 16, 17, and 18 for the end cover are then applied to obtain the following final boundary conditions for the heat balance:

$r = R_i$ for $0 < z < L_i$: inner boundary of the cylindrical wall

$$-R_i \lambda_r \frac{\partial T}{\partial r}(z,R_i,t) + \lambda_w \frac{R_e^2 - R_i^2}{2} \frac{\partial^2 T}{\partial z^2}(z,R_i,t) = \rho_w C_{pw} \frac{R_e^2 - R_i^2}{2} \frac{\partial T}{\partial t}(z,R_i,t) + R_e h\left[T(z,R_i,t) - T_a\right] \quad (26)$$

$z = 0$ for $0 < r < R_i$: inner boundary of the entrance cover

$$u(0,r,t)\rho(0,r,t)C_p T(0,r,t) - \lambda_{ax}\frac{\partial T}{\partial z}(0,r,t) = u(0,r,t)\rho_T C_p T_a + \lambda_w L_w \frac{1}{r}\frac{\partial}{\partial r}\left[r\frac{\partial T}{\partial r}(0,r,t)\right] - \rho_w C_{pw} L_w \frac{\partial T}{\partial t}(0,r,t) - h\left[T(0,r,t) - T_a\right] \quad (27)$$

$z = L_i$ for $0 < r < R_i$: inner boundary of the end cover

$$-\lambda_{ax}\frac{\partial T}{\partial z}(L_i,r,t)+\lambda_w(L_e-L_i)\frac{1}{r}\frac{\partial}{\partial r}\left[r\frac{\partial T}{\partial r}(L_i,r,t)\right]=$$

$$\rho_w C_{pw}(L_e-L_i)\frac{\partial T}{\partial t}(L_i,r,t)+h\left[T(L_i,r,t)-T_a\right]. \quad (28)$$

Numerical Discretization Scheme

A coupled set of two nonlinear partial differential equations of the parabolic type for both the mass and heat balances, with Neumann nonlinear boundary conditions, have been solved numerically. The finite difference method was applied. Moreover, a time-implicit scheme, unconditionally stable, with a constant time step throughout the numerical simulations is used. The spatial discretization scheme for the convection and diffusion terms is based on a centered finite difference scheme and is second-order accurate on a uniform grid. In order to reduce computational costs and to increase the efficiency of the numerical simulation, we used an alternate direction implicit (ADI) method, which is an example of a two-dimensional splitting method that splits the solution algorithm into two half-steps to advance one time step (Fletcher, 1991). The program was developed in the FORTRAN 77 language, and was executed with a calculation time of less than 600 s, on an iris indigo-type Silicon Graphics machine. More details concerning the numerical scheme are given in the Appendix.

Parameters and Database

Adsorbent densities

Two types of adsorbent density are taken into account. The first is the ratio of solid and gas mass to the total volume (solid and gas). This is called "apparent density of the adsorbent." However, the mass of the gas can be considered as negligible. The second one is based on the displacement of an equivalent helium volume (Malbrunot et al., 1997) called "helium density" or "solid density." It is the ratio of the solid mass to the solid-phase volume.

Porosity

The porosity distribution in fixed beds has been described by various authors (Chandrasekhara and Vortmeyer, 1979; Vortmeyer and Schuster, 1983; Govindarao and Froment, 1986; Papageorgiou and Froment, 1995; Winterberg and Tsotsas, 2000a). Their work concerns porosity distributions aimed at developing velocity profiles and modeling mass and heat transport. In our case, using the pseudohomogeneous model, porosity distribution can be considered as radially uniform because of the relatively low isosteric heat of adsorption (cf. Table 1). It has been shown that when the particle-to-bed-diameter ratio is relatively small, the pseudohomogeneous model gives reasonably good results (Vortmeyer and Michael, 1985; Winterberg and Tsotsas, 2000a).

The total porosity of the bed is the ratio of the gas volume to the total volume of the tank. It is calculated by using the apparent density and the helium density of the adsorbent:

$$\epsilon_t = 1-\frac{\rho_{\text{app}}}{\rho_s} \quad (29)$$

Table 1. 2-D Model Parameters

Gas heat capacity	14.2×10^3 J/kg·K
Solid heat capacity	725 J/kg·K
Heat capacity of the walls	468 J/kg·K
Coeff. of axial dispersion in the bed	3.4×10^{-5} m^2/s
Particle diameter	2×10^{-3} m
Coeff. of radial dispersion in the bed	3.4×10^{-5} m^2/s
Heat-transfer coeff. from walls to surrounding atm.	12 W/m^2·s
Isosteric adsorption heat	3.3×10^3 J/mol
Length of the bed and end cover of the col.	285×10^{-3} m
Inner length of the column	255×10^{-3} m
Length of the entrance cover of the col.	30×10^{-3} m
Averaged Péclet number	0.375
Universal gas constant	8.31 J/mol·K
External radius of the column	6.2×10^{-2} m
Inner radius of the column	4.8×10^{-2} m
Porosity used in the model	0.66
Micropore porosity	0.22
Total porosity	0.88
Stagnant thermal conduct. of the bed	6.9×10^{-1} W/m·K
Thermal conduct. of the gas	1.96×10^{-1} W/m·K
Thermal conduct. of the wall	13 W/m·K
Apparent density of the bed	0.24×10^3 kg/m^3
Solid density or helium density	1.99×10^3 kg/m^3
Density of the walls	7.83×10^3 kg/m^3

The porosity used in the model is less than the total porosity because we consider that there is no compression in the micropores. The microporous porosity is the ratio of the micropore volume to the total volume of the tank, and is obtained from data concerning the mass volume of micropores and by the helium density:

$$\epsilon = \epsilon_t - \epsilon_{mi}. \quad (30)$$

Velocity profile

The low ratio between particle size and tank diameter yields a flat velocity radial profile; however, the velocity decreases to zero near the wall, as pointed out in previous work on fixed beds (Chandrasekhara, and Vortmeyer, 1979; Winterberg and Tsotsas, 2000a). The axial profile is described by a linear function decreasing to zero at the end of the bed (Lamari et al., 2000), justified by the Darcy model corresponding to low *Re* numbers, which is the case in this charge process ($Re = 2$). Moreover the velocity norm is the flow rate divided by the cross section.

Coefficients of mass and heat transport

Mass diffusion is estimated based on that found in previous work on axial and radial dispersion in fixed beds (Gunn, 1987). Effective thermal conductivity is composed of a stagnant term and a dynamic term. There are various models for calculation of stagnant thermal conductivity: the Zehner and Schlünder model (Zehner and Schlünder, 1970; Froment and Bischoff, 1990), the Nozad et al. 2-D model (Nozad et al., 1985), and the contact-area model (Hsu et al., 1994). Hsu et al. (1994) have shown that when the ratio of solid thermal conductivity to thermal conductivity of the gas ranges between 1 and 10, the various models give identical results, which is also true in our case. The Zehner and Schlünder

model was used in the present work. The dynamic term is correlated with a formula developed by Winterberg et al. (2000) and Winterberg and Tsotsas (2000b), using work by Cheng and Vortmeyer (1988).

Effective axial thermal conductivity is

$$\lambda_{ax} = \lambda_{bed} + \lambda_g \frac{Pe_0}{2}. \tag{31}$$

Effective radial thermal conductivity is

$$\lambda_r = \lambda_{bed} + \lambda_g \frac{Pe_0}{8} f(R_i - r) \tag{32}$$

with

$$f(R_i - r) = \begin{cases} \left(\dfrac{R_i - r}{K_2 d_p}\right)^2 & \text{for } 0 \le R_i - r \le K_2 d_p \quad (33) \\ 1 & \text{for } K_2 d_p < R_i - r \le R_i \quad (34) \end{cases}$$

and

$$K_2 = 0.44 + 4e^{-(Pe_0/50)}. \tag{35}$$

In the present case, the pseudohomogeneous model assumption leads us to consider $f(R_i - r)$ as equal to 1.

Adsorption equilibrium and isosteric adsorption heat

The experimental setup to determine adsorption isotherms has been described previously by Malbrunot et al. (1996). The amount of adsorbed hydrogen in equilibrium in activated carbon is determined from experimental adsorption isotherms (Darkrim, private communication, 2000). They are measured at various fixed temperatures and are well described by the Radke–Prausnitz relationship (Radke and Prausnitz, 1972), which is used directly for the numerical simulation. The Radke–Prausnitz parameters are given in Table 2

$$q^*(P,T) = \frac{F \cdot K(T) \cdot P^n}{F \cdot P^{n-1} + K(T)} \tag{36}$$

with

$$K(T) = K_0 \cdot e^{-[(B \cdot \Delta H/R)T]}. \tag{37}$$

Isosteric adsorption heat is based on the Clausius–Clapeyron expression. It is calculated using adsorption isotherms at various temperatures

$$\Delta H = -RZ \left(\frac{\partial \ln P}{\partial \dfrac{1}{T}} \right)_{q^*}. \tag{38}$$

Table 2. Radke–Prausnitz Parameters

F	14.2
n	−0.199
K_0	1.23
B	9.92×10^{-6}

The range of isosteric adsorption heat is from 2,700 J/mol to 3,900 J/mol. An average value of 3,300 J/mol has been chosen. By describing isosteric adsorption heat as a linear function between 2,700 and 3,900 J/mol, the temperature profile results remain within a difference of less than 1 K. Consequently, the use of the average value for the isosteric adsorption heat is justified.

Validation of the Model and Influence of the Physical Parameters

Boundary conditions

The results of numerical simulation with the two types of boundary conditions described earlier for the 2-D model are represented by axial and radial profiles in Figures 4 and 5, respectively. In both cases, it is assumed that the external side of the column exchanges heat with the surrounding atmosphere. Whatever the boundary conditions used, the temperature range does not change by more than 0.5 K within the bed and 2 K in the vicinity of the walls. Inside the walls, the temperature gradient is almost flat, with a difference of less than 0.5 K between the inner and the external sides: the assumption of constant T_w throughout the thickness of the walls is then verified. Finally, according to these results, the "integrated boundary conditions," reducing the number of equations and the size of the grid built for the numerical simulation, as pointed out in the section on the description of the mathematical model, will be used below.

Experimental validation with surrounding atmosphere exchange

In order to validate the 2-D model according to the parameters in Table 1, three conditions of charge pressure and charge time have been used: the first at a charge pressure of 10 MPa and a charge time of 300 s, the second at 15 MPa and 300 s, and the third at 15 MPa and 400 s. The external side of the column exchanges heat with the surrounding atmosphere. The results obtained with the model have been compared with experimental results under the same conditions at the five locations in the column described earlier in the section on the experimental setup.

For the corresponding charge conditions, Figure 6 illustrates the temperature variations over 600 s, at the five positions. Good agreement was observed between the experimental and simulation results concerning the curve shape as well as for the temperature range, whatever the operating conditions and the locations. T2 and T3 are very well predicted by the model for both the time-dependant increase and decrease in temperature. They are better described than T1, T4, and T5 because the constant physical parameters necessary to the pseudohomogeneous model are easier to evaluate within the bed than near the inner side.

Analysis of different methods for heat elimination

Three methods for heat elimination were analyzed: using water cooling, using a tank wall with a higher thermal conductivity, and using an adsorbent bed, also with a much higher thermal conductivity.

The effects of heat transfers from the bed toward the outside, with the surrounding atmosphere, on the one hand, and

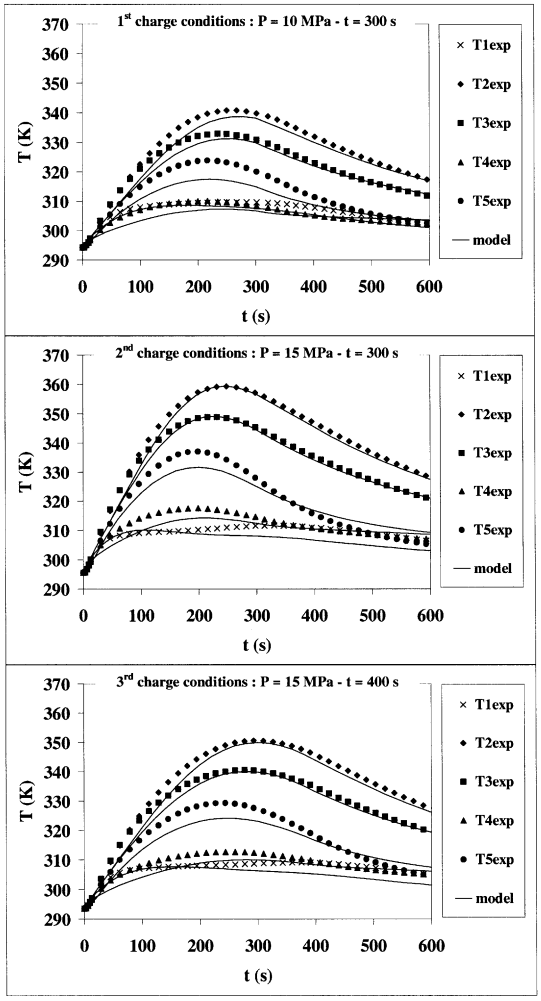

Figure 6. Experimental vs. simulation temperature variations.

with a water jacket on the other hand, have been compared. The experimental and simulation results, obtained in the case of the second charge conditions (charge pressure of 15 MPa and charge time of 300 s) and for only three positions in the column, are shown in Figure 7. The temperature increase stage as well as the maximum do not depend on the external heat-transfer efficiency. There is a slightly higher decrease stage with the water jacket; at $t = 600$ s, the temperature is cooler by about 2 K than when using the surrounding atmosphere for the cooling procedure. These results are verified for both the experimental and simulation results. This behavior shows that the heat produced during the charge time cannot be pumped out by acting only on the external heat exchange. This is corroborated by the comparison of maximal temperature and temperature at the wall for both the surrounding atmosphere and the water jacket, as shown in Table 3, lines 1 and 2. The difference between these two types of heat exchange is only near the walls, the maximum temperature of the bed being unchanged during the charge time.

Another way to change the heat flow across the walls is to choose another material than stainless steel for the tank.

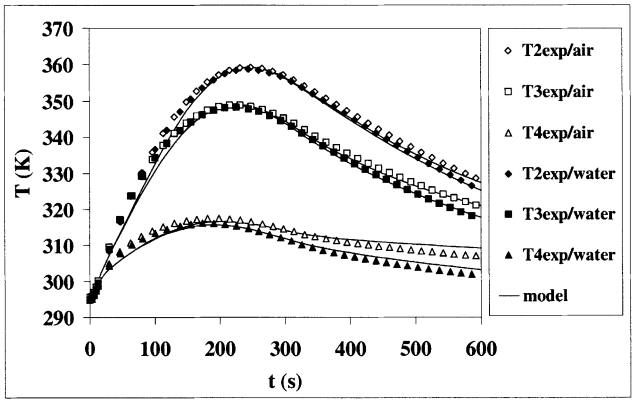

Figure 7. Comparison of temperature variations with surrounding atmosphere exchange and water cooling exchange, for second charge conditions.

Copper is a good candidate due to its high thermal conductivity. Numerical simulations were performed with the thermal conductivity of copper; however, in order to take into account its weaker mechanical resistance compared to stainless steel, the thickness of the wall had to be increased by 0.028 m. The results of numerical simulation obtained for a charge setup with a charge pressure of 15 MPa and a charge time of 300 s, with a copper tank, are presented in Table 3, line 3. As was observed previously, when cooling was performed with water instead of the surrounding atmosphere, the only difference in the temperatures obtained with the stainless steel and copper walls is observed in the vicinity of the walls, because the heat-flow resistance is located within the bed due to its low thermal conductivity.

In order to decrease the maximum temperature, a method must be found for directly extracting the heat produced within the bed. Since heat flow resistance appears to be located inside the bed itself, one way to reduce the temperature increase would be to use an adsorbent bed with much higher thermal conductivity. The results obtained by the numerical simulation of a hydrogen charge in a tank filled with an adsorbent bed with thermal conductivities of 1.8 W/m/K and 13.6 W/m/K for the axial and the radial components, respectively, are presented in Table 3, line 4. These values are those reported for an activated carbon adsorbent bed, the grains of which have been mechanically consolidated and the thermal conductivity of which has been increased by mixing these pro-

Table 3. Comparison of Maximum Temperature, Temperature at the Wall, and H_2 Loaded for Various Cases, for Second Charge Conditions

Cases	T_{max} K	$T_{at\ the\ wall}$ K	H_2 Loaded (kg/m^3)
Steel wall—air exchange (basic case)	359.1	305.9	10.92
Steel wall—water jacket	359.0	300.2	11.00
Copper wall—air exchange	358.8	297.1	11.02
Steel wall—air exchange High conduct. of the bed	310.3	307.8	11.63
Optimized tank	304.0	300.3	11.86

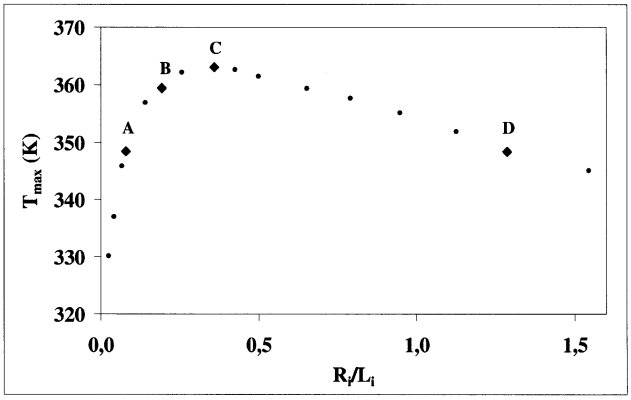

Figure 8. Influence of the geometry on the maximum temperature in the bed at $t = 260$ s, for second charge conditions: (A) industrial bottle; (B) experimental column; (C) worst geometry; (D) flat tank.

tected grains with expanded natural graphite (GNE). The mixture is then compressed. This process was developed by Olives and Mauran (2001) and Biloé et al. (2001). Simulation of this system shows the considerable advantage in using such a bed. In fact, a marked decrease in temperature is observed. The maximum varies from 359.1 K, with a classic bed, down to 310.5 K, with this new adsorbent bed. Increasing the axial thermal conductivity to 13.6 W/m·K, however, does not affect the maximum temperature, which decreases by not more than 0.5 K due to the low radius-to-length ratio considered here.

Influence of the column geometry

Considering the homogeneous temperature within the tank, with a given inner volume, one can find the minimum heat exchange at the walls by minimizing the inner surface area of the heat exchange written as a function of the inner radius of the column. The derivative function is equal to zero for the radius, called R_i^*, corresponding to the minimum heat exchange at the walls. Replacing the inner volume by the well-known formula for a cylinder yields a simple relationship between R_i^* and the corresponding inner length L_i^*

$$\frac{R_i^*}{L_i^*} = 0.5. \tag{40}$$

The 2-D model was used to simulate the influence of tank geometry on the bed temperature profiles. Figure 8 represents variations in the maximum temperature, T_{max} (at $t = 260$ s), in the bed during a charge setup with a charge pressure of 15 MPa and a charge time of 300 s, as a function of the radius-to-length ratio. The maximum does not occur at $R_i/L_i = 0.5$, but rather at $R_i/L_i = 0.36$. The existence of thermal gradients in the bed may explain this phenomenon. In fact, this value of the radius-to-length ratio corresponds to the worst geometry for heat exchange between the column and the surrounding atmosphere. Point A represents a long bottle

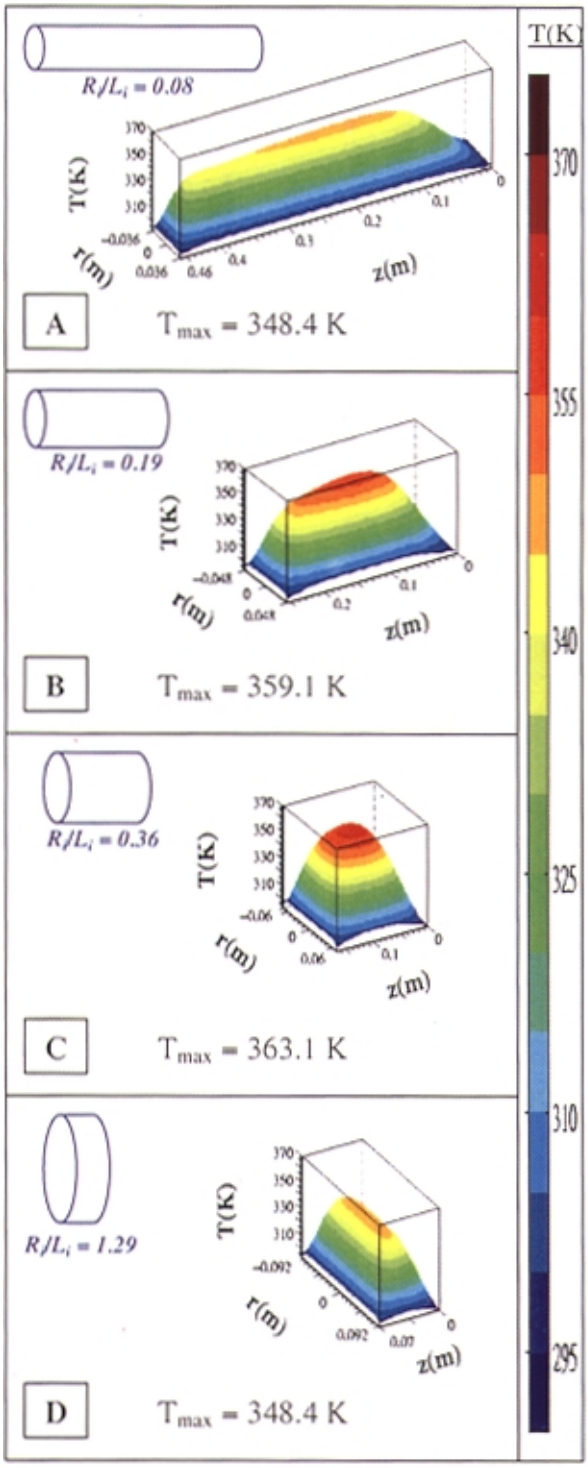

Figure 9. 3-D profiles at $t = 260$ s, for second charge conditions: (A) industrial bottle; (B) experimental column; (C) worst geometry; (D) flat tank.

(industrial type), point B the experimental column, point C the worst geometry, and point D a flat tank, with the same maximum temperature as the long bottle. Figure 9 shows 3-D representations for each case. The temperature is predictably

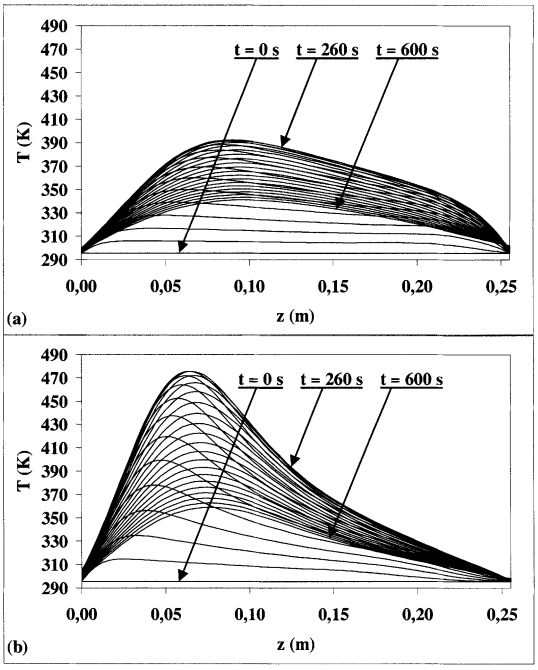

Figure 10. Axial profiles over 600 s, for second charge conditions: (a) twofold higher adsorption; (b) fourfold higher adsorption.

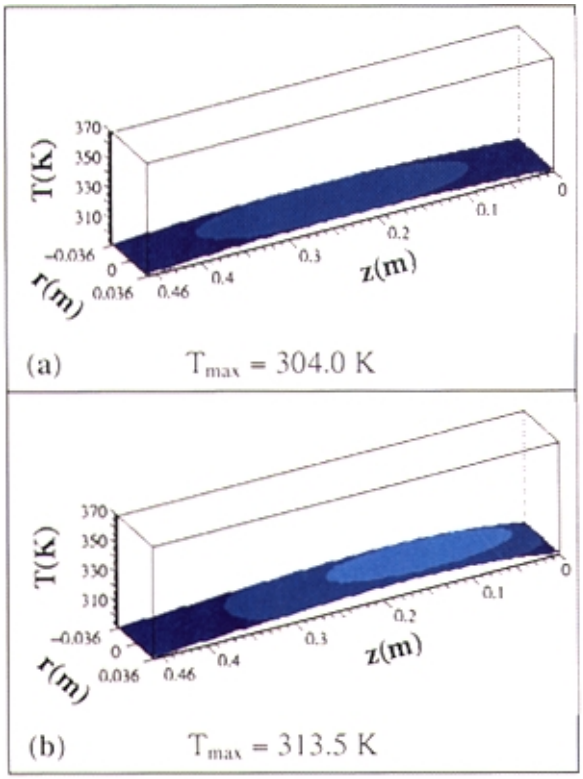

Figure 11. 3-D profiles at $t = 260$ s, for second charge conditions in optimized tank: (a) actual adsorption; (b) fourfold higher adsorption.

lower in cases A and D. One can see that strong axial and radial profiles are still present in the vicinity of the walls, even with a long column or a flat tank. However, axial profiles are flat in the axial midzone for the long bottle, and the radial profile is flat in the radial midzone for the flat tank. Therefore, the further apart the walls are, the flatter the profiles.

Influence of the adsorption equilibrium

The effect of adsorption capacity has been studied with a charge pressure of 15 MPa and a charge time of 300 s, as well as the thermal conductivities of the bed given in Table 1. Results of simulations performed with adsorption capacity multiplied by 2 and 4 are presented in Figure 10. The axial profiles show an increase in the maximum temperature due to greater adsorption heat effects. Furthermore, the maximum shifts toward the entrance of the tank due to the higher consumption of gas in the bed.

Optimization of the Column

Analysis of the influence of the various parameters shows that optimal storage could be obtained with an optimized column having a water jacket, copper walls, a radius-to-length ratio corresponding to a long industrial bottle and high thermal conductivity of the bed in the radial direction (13.6 W/m·K). Figure 11 shows 3-D representations for an optimized tank under second charge conditions (charge pressure of 15 MPa and charge time of 300 s), with the actual adsorption capacity and with an adsorption capacity multiplied by a factor of 4. It can be seen that under optimized conditions (water jacket, copper walls, long bottle, and thermal conductivity in the radial direction of 13.6 W/m·K), the maximum temperature can be considerably reduced. Maximum temperature and temperature at the wall for the basic case and the optimized tank with the actual adsorption are presented in lines 1 and 5 of Table 3, respectively.

As pointed out in previous works (Berry and Aceves, 1998), 5 kg of H_2 onboard are needed to drive 500 km under normal conditions. So, the DOE standard of 63 kg/m^3 is respected for a tank volume of about 80 L. Given that the optimized tank is able to store 11.9 kg/m^3, as shown in Table 3, line 5, its volume must be about 425 L. This kind of tank could be designed to sit on the vehicle roof.

Conclusion

A 2-D model for the nonisothermal storage of hydrogen by adsorption at moderate pressure (15 MPa) has been developed. This model, which is based on the Equilibrium Theory of Adsorption, describes axial and radial thermal flows inside an adsorbent bed filled with molecular hydrogen. For the numerical simulation, the flat radial velocity profile is considered; however, the velocity decreases to zero near the wall. Moreover, the axial profile is described by a linear function decreasing to zero at the end of the bed. An average value for isosteric adsorption heat is used, as is the thermal conductivity of the bed. Two different approaches to describing thermal flow across the walls have been presented. The first

one is a complete model with a separate equation for the thermal balance in the walls. The second approach includes the thermal balance of the walls in the boundary conditions of the bed, assuming a uniform temperature throughout the thickness of the walls. Comparison of the numerical results for the two cases shows that the maximal difference is less than 0.5 K within the bed and 2 K in the vicinity of the walls. Based on these results, the second model was chosen due to the reduction in the number of equations and the size of the grid built for the numerical simulation.

This model has been validated using temperature measurements performed in an experimental facility. This allows variations of axial and radial temperature fields at five different locations within the tank to be measured. The experimental and simulation results for the axial and radial profiles were systematically compared at various times and locations. Reasonably good agreement was obtained.

Experiments and numerical simulation designed to reduce heating of the bed during hydrogen filling were also developed. Results showed that the increase in the heat-transfer coefficient from the walls to the surrounding atmosphere by the use of a water jacket or by changing the wall material did not affect the maximum temperature within the bed, while an adsorbent bed with relatively low thermal conductivities is used.

Finally, it has been observed that the best way to increase heat transfer toward the outside is to choose a more favorable geometry for the column (radius-to-length ratio) and to increase the thermal flow of the bed, essentially in the direction of the largest exchange surface. This can be done by increasing the thermal conductivity of the adsorbent in the right direction or by adding supplementary interbed heat exchangers, such as fins, to the system. The optimized tank is thus able to store a sufficient amount of H_2 to enable a vehicle to travel 500 km on one charge, provided the volume is about 425 L. A more sophisticated model, taking into account the mass transfer inside the adsorbent particles and variable physical parameters such as porosity near the walls, must be developed to determine the optimal filling conditions.

Acknowledgments

We acknowledge Pr. Anne-Sophie Lamine for her help. Dr. Farida Darkrim is thanked for adsorption isotherms. We also thank Graham Smith for English language corrections.

Notation

C_p = gas heat capacity, J/kg·K
C_{ps} = solid heat capacity, J/kg·K
C_{pw} = heat capacity of the walls, J/kg·K
D_{ax} = coefficient of axial dispersion in the bed, m^2/s
d_p = particle diameter, m
D_r = coefficient of radial dispersion in the bed, m^2/s
h = heat-transfer coefficient from walls to surrounding atmosphere, W/m^2·s
K_2 = damping parameter
L_e = length of the bed and the end cover of the column, m
L_i = inner length of the column, m
L_i^* = theoretical inner length of the column for minimum heat exchange, m
L_w = length of the entrance cover of the column, m
q^* = amount of adsorbed gas in equilibrium, mol/kg
P = pressure, Pa
P_0 = pressure at $t = 0$, Pa
Pe_0 = average molecular Péclet number [$Pe_0 = (\bar{u} d_p \rho C_p)/\lambda_g$]
R = universal gas constant, J/mol·K
Re = Reynolds number
R_e = external radius of the column, m
R_i = inner radius of the column, m
R_i^* = theoretical inner radius of the column for minimum heat exchange, m
r = radial position in the bed, m
t = time, s
T = temperature of the bed, K
T_a = room temperature, K
T_{max} = maximum temperature of the bed, K
T_w = temperature of the wall and the covers, K
u = superficial gas velocity, m/s
$\bar{u}$ = average superficial gas velocity, m/s
z = axial position in the bed, m
Z = compressibility factor

Greek letters

ΔH = isosteric adsorption heat, J/mol
ϵ = porosity used in the model
ϵ_{mi} = micropore porosity
ϵ_t = total porosity
λ_{ax} = effective axial thermal conductivity of the bed, W/m·K
λ_b = stagnant thermal conductivity of the bed, W/m·K
λ_g = thermal conductivity of the gas, W/m·K
λ_r = effective radial thermal conductivity of the bed, W/m·K
λ_w = thermal conductivity of the walls, W/m·K
ρ = gas density, kg/m^3
ρ_0 = gas density at $t = 0$, kg/m^3
ρ_{app} = apparent density of the bed, kg/m^3
ρ_s = solid density or helium density, kg/m^3
ρ_T = gas density in the charge circuit, kg/m^3
ρ_w = density of the walls, kg/m^3

Literature Cited

Barbosa Mota, J. P., "Modélisation des Transferts Couplés en Milieux Poreux," PhD Thesis, INPL, Nancy, France (1995).
Barbosa Mota, J. P., A. E. Rodrigues, E. Saatdjian, and D. Tondeur, "Dynamics of Natural Gas Adsorption Storage Systems Employing Activated Carbon," *Carbon*, **35**, 12459 (1997).
Berry, D. G., and M. S. Aceves, "On-Board Storage Alternatives for Hydrogen Vehicles," *Energy Fuels*, **12**, 49 (1998).
Biloé, S., V. Goetz, and S. Mauran, "Dynamic Discharge and Performance of a New Adsorbent for Natural Gas Storage," *AIChE J.*, **47**, 2819 (2001).
Chandrasekhara, B. C., and D. Vortmeyer, "Flow Model for Velocity Distribution in Fixed Porous Beds Under Isothermal Conditions," *Wärme- und Soffübertragung*, **12**, 105 (1979).
Cheng, P., and D. Vortmeyer, "Transverse Thermal Dispersion and Wall Channelling in a Packed Bed with Forced Convective Flow," *Chem. Eng. Sci.*, **43**, 2523 (1988).
Chihara, K., and M. Suzuki, "Simulation of Nonisothermal Pressure Swing Adsorption," *J. Chem. Eng. Jpn.*, **16**, 53 (1983).
Das, L. M., "On-Board Hydrogen Storage Systems for Automotive Application," *Int. J. Hydrogen Energy*, **21**, 789 (1996).
Dresselhaus, M. S., K. A. Williams, and P. C. Eklund, "Hydrogen Adsorption in Carbon Materials," *MRS Bull.*, **24**, 45 (1999).
Farooq, S., M. M. Hassan, and D. M. Ruthven, "Heat Effects in Pressure Swing Adsorption," *Chem. Eng. Sci.*, **43**, 1017 (1988).
Farooq, S., and D. M. Ruthven, "Heat Effects in Adsorption Column Dynamics: 1. Comparison of One- and Two-Dimensional Models," *Ind. Eng. Chem. Res.*, **29**, 1076 (1990).
Fletcher, C. A. J., *Computational Techniques for Fluid Dynamics*, Vols. 1, 2, Springer-Verlag, Berlin (1991).
Froment, G. F., and K. B. Bischoff, *Chemical Reactor Analysis and Design*, Wiley, New York (1990).
Govindarao, V. M. H., and G. F. Froment, "Voidage Profiles in Packed Beds of Spheres," *Chem. Eng. Sci.*, **41**, 533 (1986).

Gunn, D. J., "Axial and Radial Dispersion in Fixed Beds," *Chem. Eng. Sci.*, **42**, 363 (1987).
Hsu, C. T., P. Cheng, and K. W. Wong, "Modified Zehner-Schlünder Models for Stagnant Thermal Conductivity of Porous Media," *Int. J. Heat Mass Transfer*, **37**, 2751 (1994).
Hynek, S., W. Fuller, and J. Bentley, "Hydrogen Storage by Carbon Sorption," *Int. J. Hydrogen Energy*, **22**, 601 (1997).
Kikkinides, E. S., and R. T. Yang, "Effects of Bed Pressure Drop on Isothermal and Adiabatic Adsorber Dynamics," *Chem. Eng. Sci.*, **48**, 1545 (1993).
Knaebel, K. S., and F. B. Hill, "Analysis of Gas Purification by Pressure Swing Adsorption: Priming the Parametric Pump," *Sep. Sci. Technol.*, **18**, 1193 (1983).
Knaebel, K. S., and F. B. Hill, "Pressure Swing Adsorption: Development of an Equilibrium Theory for Gas Separations," *Chem. Eng. Sci.*, **40**, 2351 (1985).
Lamari, M., "Procédé de Stockage de l'Hydrogène par Adsorption: Modélisation des Effets Thermiques au Remplissage et Vidage d'un Réservoir et Comparaison à l'Expérience," PhD Thesis, Université Paris 13, Villetaneuse, France (2000).
Lamari, M., A. Aoufi, and P. Malbrunot, "Thermal Effects in Dynamic Storage of Hydrogen by Adsorption," *AIChE J.*, **46**, 632 (2000).
Malbrunot, P., D. Vidal, and J. Vermesse, "Storage of Gases at Room Temperature by Adsorption at High Pressure," *Appl. Therm. Eng.*, **16**, 375 (1996).
Malbrunot, P., D. Vidal, J. Vermesse, R. Chahine, and T. K. Bose, "Adsorbent Helium Density Measurement and Its Effect on Adsorption at High Pressure," *Langmuir*, **13**, 539 (1997).
Nicholetti, G., "The Hydrogen Option for Energy: A Review of Technical, Environmental and Economic Aspects," *Int. J. Hydrogen Energy*, **20**, 759 (1995).
Noh, J. S., R. K. Agawal, and J. A. Schwartz, "Hydrogen Storage Using Activated Carbon," *Int. J. Hydrogen Energy*, **12**, 693 (1987).
Nozad, S., R. G. Carbonell, and S. Whitaker, "Heat Conduction in Multiphase Systems: I. Theory and Experiments for Two-Phase Systems," *Chem. Eng. Sci.*, **40**, 843 (1985).
Olives, R., and S. Mauran, "A Highly Conductive Porous Medium for Solid-Gas Reactions: Effect of the Dispersed Phase on the Thermal Tortuosity," *Transp. Porous Media*, **43**, 377 (2001).
Papageorgiou, J. N., and G. F. Froment, "Simulation Models Accounting for Radial Voidage Profiles in Fixed-Bed Reactors," *Chem. Eng. Sci.*, **50**, 3043 (1995).
Radke, C. J., and J. M. Prausnitz, "Thermodynamics of Multi-Solute Adsorption from Dilute Solutions," *AIChE J.*, **18**, 761 (1972).
Ruthven, D. M., S. Farooq, and K. S. Knaebel, *Pressure Swing Adsorption*, VCH, New York (1994).
Vortmeyer, D., and J. Schuster, "Evaluation of Steady Flow Profiles in Rectangular and Circular Packed Beds by a Variational Method," *Chem. Eng. Sci.*, **38**, 1691 (1983).
Vortmeyer, D., and K. Michael, "The Effect of Non-Uniform Flow Distribution on Concentration Profiles and Breakthrough Curves of Fixed Bed Adsorbers," *Chem. Eng. Sci.*, **40**, 2135 (1985).
Winterberg, M., E. Tsotsas, A. Krischke, and D. Vortmeyer, "A Simple and Coherent Set of Coefficients for Modelling of Heat and Mass Transport With and Without Chemical Reaction in Tubes Filled With Spheres," *Chem. Eng. Sci.*, **55**, 967 (2000).
Winterberg, M., and E. Tsotsas, "Impact of Tube-to-Particle-Diameter Ratio on Pressure Drop in Packed Beds," *AIChE J.*, **46**, 1084 (2000a).
Winterberg, M., and E. Tsotsas, "Modelling of Heat Transport in Beds Packed with Spherical Particles for Various Bed Geometries and/or Thermal Boundary Conditions," *Int. J. Therm. Sci.*, **39**, 556 (2000b).
Zehner, P., and E. U. Schlünder, "Wärmeleitfähigkeit von Schüttungen bei Mässigen Temperaturen," *Chem. Ing. Tech.*, **42**, 933 (1970).
Zhong, G. M., F. Meunier, S. Huberson, and J. B. Chalfen, "Pressurization of a Single-Component Gas in an Adsorption Column," *Chem. Eng. Sci.*, **47**, 543 (1992).
Zoghlami-Mosrati, H., "Etude des Transferts et Ecoulement Réactifs en Milieu Poreux: Application à un Stockage de Solides Thermiquement Instables," PhD Thesis, INPL, Nancy, France (1999).

Appendix: Description of the Numerical Scheme

In order to simplify the description of the numerical scheme, mass balance (Eq. 1) can be rewritten:

$$\frac{\partial \rho}{\partial t} = L_r(\rho) + L_z(\rho) + S_\rho(\rho, T), \tag{A1}$$

where

$$L_r(\rho) = \frac{D_r}{r}\frac{\partial}{\partial r}\left(r\frac{\partial \rho}{\partial r}\right) \tag{A2}$$

$$L_z(\rho) = \frac{\partial}{\partial z}\left(D_z\frac{\partial \rho}{\partial z} - \rho\frac{u}{\epsilon}\right) \tag{A3}$$

$$S_\rho(\rho, T) = -\frac{1-\epsilon}{\epsilon}\rho_s M_{H_2}\frac{\partial q^*}{\partial t}. \tag{A4}$$

The heat balance (Eq. 2) can be rewritten:

$$\frac{\partial (f(\rho)T)}{\partial t} = M_r(T) + M_z(\rho, T) + S_T(\rho, T) \tag{A5}$$

where

$$f(\rho) = \rho Cp + \frac{1-\epsilon}{\epsilon}\rho_s Cp_s - \rho\frac{R}{M} \tag{A6}$$

$$M_r(T) = \frac{\lambda_r}{\epsilon r}\frac{\partial}{\partial r}\left(r\frac{\partial T}{\partial r}\right) \tag{A7}$$

$$M_z(\rho, T) = \frac{\partial}{\partial z}\left(\frac{\lambda_z}{\epsilon}\frac{\partial T}{\partial z} - \rho\frac{u}{\epsilon}CpT\right) \tag{A8}$$

$$S_T(\rho, T) = \frac{1-\epsilon}{\epsilon}\rho_s \Delta H\frac{\partial q^*}{\partial t}. \tag{A9}$$

During the first half-step, implicit discretization is performed along the z-axis for both mass and heat balances. The discretized equation for mass balance is rewritten as

$$\frac{\rho_{ij}^{n+(1/2)}}{\Delta t/2} - L_z\left(\rho_{ij}^{n+(1/2)}\right) = \frac{\rho_{ij}^{n}}{\Delta t/2} + L_r\left(\rho_{ij}^{n}\right) + S_\rho\left(\rho_{ij}^{n+(1/2)}, T_{ij}^{n+(1/2)}\right). \tag{A10}$$

The discretized equation for heat balance is rewritten as

$$\frac{f\left(\rho_{ij}^{n+(1/2)}\right)T_{ij}^{n+(1/2)}}{\Delta t/2} - M_z\left(\rho_{ij}^{n+(1/2)}, T_{ij}^{n+(1/2)}\right) = \frac{f\left(\rho_{ij}^{n}\right)T_{ij}^{n}}{\Delta t/2} + M_r\left(T_{ij}^{n}\right) + S_T\left(\rho_{ij}^{n+(1/2)}, T_{ij}^{n+(1/2)}\right). \tag{A11}$$

The treatment of the boundary conditions is crucial for the accuracy of the ADI procedure with respect to the equation

over the interval $[t_n, t_{n+1}]$. We have to evaluate for $z = 0$ and $z = H$, $\partial\rho/\partial z$ and $\partial T/\partial z$ at time $t_{n+(1/2)}$, and for $r = 0$ and $r = R$, $\partial\rho/\partial r$ and $\partial T/\partial r$ at time t_n.

During the second half-step, implicit discretization is performed along the r-axis for both the heat and the mass balances, but uses the fields $(T_{ij}^{n+(1/2)}, \rho_{ij}^{n+(1/2)})$ determined at the end of the first half-step. The same methodology as in the previous case of discretization along the z-axis is applied to obtain both the mass and enthalpy balances:

$$\frac{\rho_{ij}^{n+(1/2)}}{\Delta t/2} - L_z\left(\rho_{ij}^{n+(1/2)}\right) = \frac{\rho_{ij}^{n}}{\Delta t/2} + L_r\left(\rho_{ij}^{n}\right) + S_\rho\left(\rho_{ij}^{n+(1/2)}, T_{ij}^{n+(1/2)}\right) \quad \text{(A12)}$$

$$\frac{f\left(\rho_{ij}^{n+(1/2)}\right)T_{ij}^{n+(1/2)}}{\Delta t/2} - M_z\left(\rho_{ij}^{n+(1/2)}, T_{ij}^{n+(1/2)}\right) = \frac{f\left(\rho_{ij}^{n}\right)T_{ij}^{n}}{\Delta t/2} + M_r\left(T_{ij}^{n}\right) + S_T\left(\rho_{ij}^{n+(1/2)}, T_{ij}^{n+(1/2)}\right). \quad \text{(A13)}$$

During each half-step, an iterative method for the solution of the nonlinear set of equations in a decoupled manner is used, that is, the mass balance is first solved, then the heat balance, instead of solving the overall nonlinear system at the same time. A stopping criterion for the iterative numerical procedure is based on the computation of the relative error between two consecutive solutions for both the mass and heat balances.

Manuscript received Oct. 3, 2001, and revision received Feb. 4, 2002.